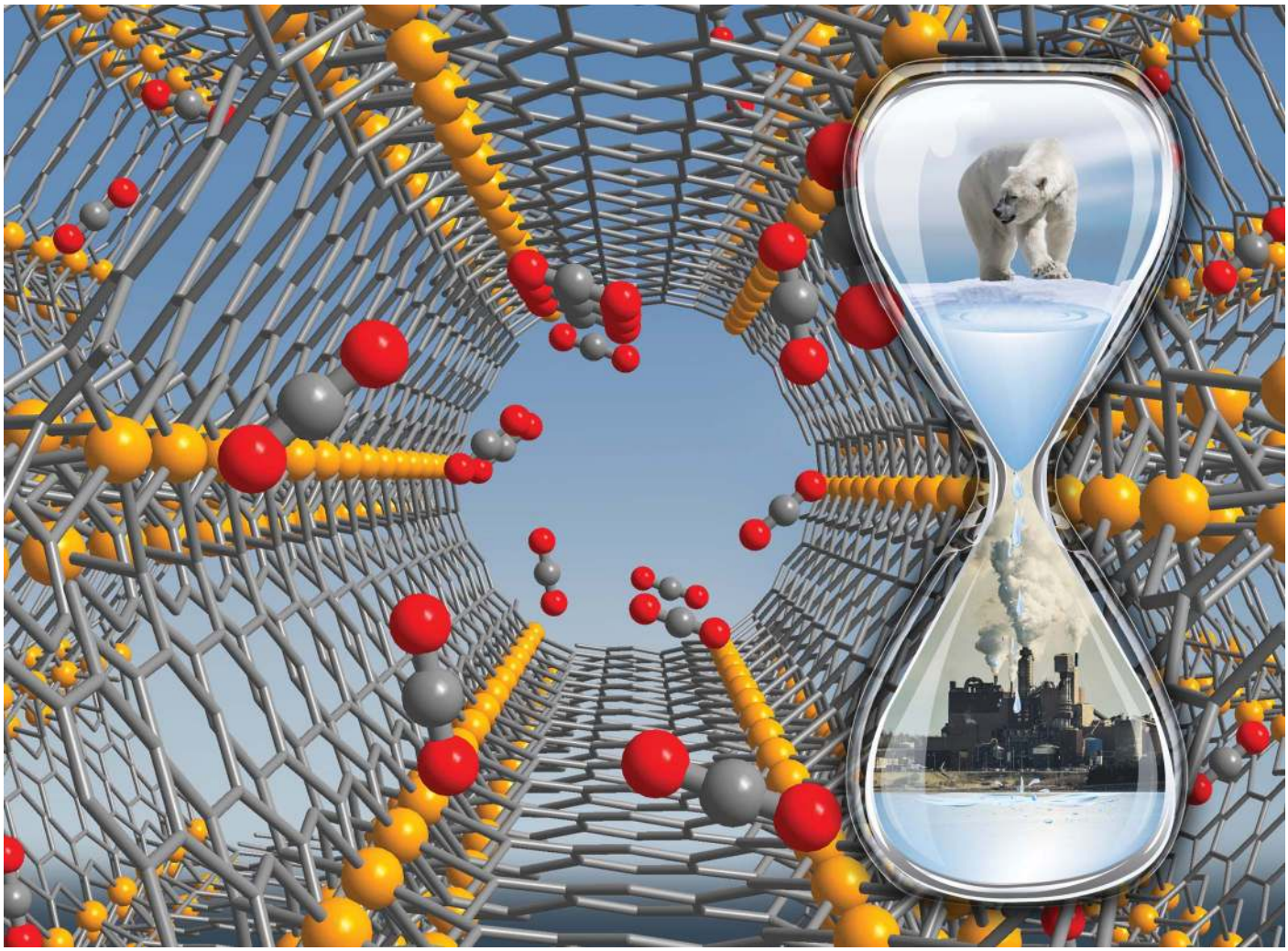

Showcasing research from the Laboratory of Wendy L. Queen at the Molecular Foundry located at Lawrence Berkeley National Laboratory in Berkeley, California.

Comprehensive study of carbon dioxide adsorption in the metal-organic frameworks M_2(dobdc) (M = Mg, Mn, Fe, Co, Ni, Cu, Zn)

The results reveal important, molecular level detail of CO_2 binding in a prominent family of Metal-Organic Frameworks whose adsorption properties can be readily tuned with metal-substitution. This information, which is of significant importance in the context of carbon capture, allows us to make a detailed comparison with DFT calculations; theoretical results show excellent agreement with experimental determination of intramolecular CO_2 angles, CO_2 binding geometries, and isosteric heats of CO_2 adsorption.

Credit: PA Creative, Lawrence Berkeley National Laboratory

As featured in:

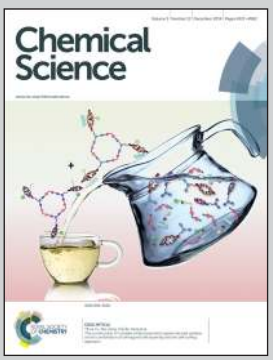

See Wendy L. Queen, Craig M. Brown *et al.*, *Chem. Sci.*, 2014, **5**, 4569.

ROYAL SOCIETY OF CHEMISTRY

www.rsc.org/chemicalscience

Registered charity number: 207890

Chemical Science

EDGE ARTICLE

View Article Online
View Journal | View Issue

Cite this: *Chem. Sci.*, 2014, **5**, 4569

Comprehensive study of carbon dioxide adsorption in the metal–organic frameworks M_2(dobdc) (M = Mg, Mn, Fe, Co, Ni, Cu, Zn)†

Wendy L. Queen,*[a] Matthew R. Hudson,‡[b] Eric D. Bloch,‡[c] Jarad A. Mason,[c] Miguel I. Gonzalez,[c] Jason S. Lee,[ad] David Gygi,[c] Joshua D. Howe,[ad] Kyuho Lee,[ad] Tamim A. Darwish,[e] Michael James,[ef] Vanessa K. Peterson,[g] Simon J. Teat,[h] Berend Smit,[dij] Jeffrey B. Neaton,[ak] Jeffrey R. Long[ci] and Craig M. Brown*[bl]

Analysis of the CO_2 adsorption properties of a well-known series of metal–organic frameworks M_2(dobdc) (dobdc^{4-} = 2,5-dioxido-1,4-benzenedicarboxylate; M = Mg, Mn, Fe, Co, Ni, Cu, and Zn) is carried out in tandem with *in situ* structural studies to identify the host–guest interactions that lead to significant differences in isosteric heats of CO_2 adsorption. Neutron and X-ray powder diffraction and single crystal X-ray diffraction experiments are used to unveil the site-specific binding properties of CO_2 within many of these materials while systematically varying both the amount of CO_2 and the temperature. Unlike previous studies, we show that CO_2 adsorbed at the metal cations exhibits intramolecular angles with minimal deviations from 180°, a finding that indicates a strongly electrostatic and physisorptive interaction with the framework surface and sheds more light on the ongoing discussion regarding whether CO_2 adsorbs in a linear or nonlinear geometry. This has important implications for proposals that have been made to utilize these materials for the activation and chemical conversion of CO_2. For the weaker CO_2 adsorbents, significant elongation of the metal–O(CO_2) distances are observed and diffraction experiments additionally reveal that secondary CO_2 adsorption sites, while likely stabilized by the population of the primary adsorption sites, significantly contribute to adsorption behavior at ambient temperature. Density functional theory calculations including van der Waals dispersion quantitatively corroborate and rationalize observations regarding intramolecular CO_2 angles and trends in relative geometric properties and heats of adsorption in the M_2(dobdc)–CO_2 adducts.

Received 12th July 2014
Accepted 28th August 2014

DOI: 10.1039/c4sc02064b

www.rsc.org/chemicalscience

Introduction

Currently, 80% of global energy is supplied by carbon-based fossil fuels,[1] which has led to concerns over the environmental impact of increasing atmospheric CO_2 levels and has sparked ever-growing interest in renewable energy sources. As energy transitions are historically slow, the need for mitigation of current CO_2 emissions using carbon capture and sequestration (CCS) is becoming more evident;[2,3] however, this task is currently constrained by the development of adequate gas

[a]*The Molecular Foundry, Lawrence Berkeley National Laboratory, Berkeley, California, 94720, USA. E-mail: wlqueen@lbl.gov; Tel: +1 5104865526*

[b]*National Institute of Standards and Technology, Center for Neutron Research, Gaithersburg, Maryland, 20899, USA. E-mail: craig.brown@nist.gov; Tel: +1 3019755134*

[c]*Department of Chemistry, University of California, Berkeley, California, 94720-1462, USA. E-mail: jrlong@berkeley.edu; Tel: +1 5106420860*

[d]*Department of Chemical and Biomolecular Engineering, University of California, Berkeley, California, 94720-1462, USA*

[e]*National Deuteration Facility, Australian Nuclear Science and Technology Organisation, Lucas Heights, Australia*

[f]*Australian Synchrotron, 800 Blackburn Road, Clayton, VIC 3168, Australia*

[g]*The Bragg Institute, Australian Nuclear Science and Technology Organisation, Lucas Heights, NSW 2234, Australia*

[h]*Advanced Light Source, Lawrence Berkeley National Laboratory, Berkeley, California, 94720, USA*

[i]*Division of Materials Sciences, Lawrence Berkeley National Laboratory, Berkeley, California, 94720, USA*

[j]*Department Institut des Sciences et Ingénierie Chimiques, Ecole Polytechnique Fédérale de Lausanne (EPFL), CH 1015 Lausanne, Switzerland*

[k]*Department of Physics, University of California, Berkeley, California, 94720-1462, USA*

[l]*Department of Chemical Engineering, University of Delaware, Newark, Delaware, 19716, USA*

† Electronic supplementary information (ESI) available: Adsorption isotherms and fits, crystallographic information, inelastic scattering data, additional figures, Fourier difference maps, and results from DFT simulations. CCDC 1002993–1003002 and 1003008–1003015. For ESI and crystallographic data in CIF or other electronic format see DOI: 10.1039/c4sc02064b

‡ These authors contributed equally to this study.

separation technologies. While CO_2 capture from air is not very practical,[4,5] that of large point sources, such as coal-fired power plants, could be realized.[6] These sources account for more than 40% of global CO_2 emissions.[7] The most mature capture technology involves aqueous amine-based scrubbers, whose implementation is hampered in particular by high energy costs for regeneration.[8] It is projected that use of physical adsorbents with lower regeneration energy requirements, such as metal–organic frameworks, could reduce the parasitic loss associated with current capture technologies, which is as high as 15–30% of the total output of a power plant.[9] Metal–organic frameworks are particularly attractive as their adsorption properties can be readily tuned by chemical modification to give adsorbents with high capacities and selectivities for small guest molecules.[10,11]

Recently, we synthesized an iron(II) containing metal–organic framework, Fe_2(dobdc) (dobdc^{4-} = 2,5-dioxido-1,4-benzenedicarboxylate).[12] This material belongs to an extensive family of compounds alternatively known as M-MOF-74 or CPO-27-M, where M = Mg, Mn, Fe, Co, Ni, Cu, or Zn.[12–20] The number of metal cations that can be incorporated into this isostructural series of frameworks is only rivalled by its sodalite counterpart, M-BTT (BTT^{3-} = 1,3,5-benzenetristetrazolate), where M = Mn, Fe, Co, Ni, Cu or Cd,[21–24] and M_3(btc)$_2$ (btc^{3-} = 1,3,5-benzenetricarboxylate), where M = Cr, Cu, Zn, Mo, or Ru.[25–29]

The M_2(dobdc) structure type features one-dimensional metal oxide chains that are connected by dobdc^{4-} ligands to form a hexagonal array of channels, approximately 11 Å across (Fig. 1) that propagate along the crystallographic *c*-axis. The high negative charge on the compact dobdc^{4-} ligand leads to a greater density of metal cations than found in most metal–organic frameworks with such large pores. Heating the material under dynamic vacuum liberates a solvent molecule from each metal, leaving behind square pyramidal metal cations that have an open coordination site directed into the channel. The presence of highly reactive, electron deficient metals is proven to be an effective means of inducing framework selectivity for gas adsorption, enhancing the surface packing density of adsorbates, and providing reactive sites for facilitating chemical reactions on the framework surface.[12,30–33]

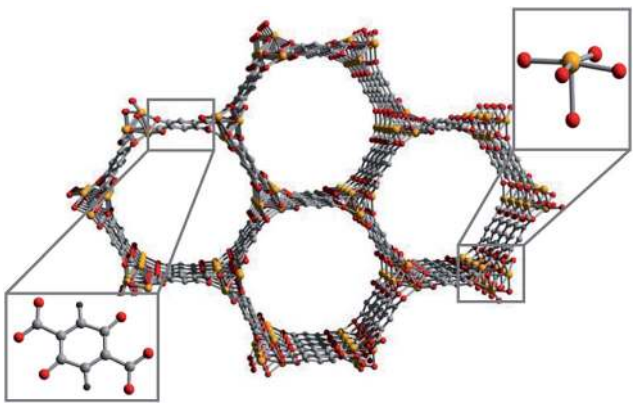

Fig. 1 Ball and stick model of the M_2(dobdc) structure type showing the MO_5 polyhedron and (dobdc)$^{4-}$ linker. Orange, red, grey, and black spheres represent the metal, oxygen, carbon, and hydrogen, respectively.

Wide spread interest in Mg_2(dobdc) for pre- and post-combustion CO_2 capture technologies[34–36] has led us to investigate the CO_2 adsorption properties of the iron(II) containing analog. Since all M_2(dobdc) frameworks are highly crystalline, this material family offers a rare opportunity for detailed studies of the relationships between structure and adsorption properties.[37] As a result, we further draw comparisons between several of its isostructural counterparts and show the first full report coupling both CO_2 adsorption properties with a detailed structural analysis of this extensive family (where M = Mg, Mn, Fe, Co, Ni, Cu, or Zn). Since structure dictates function, *in situ* structural characterization of frameworks with adsorbed gas species can be used to improve our understanding of the structural properties necessary to optimize a framework for carbon capture purposes. In this study we have gained detailed molecular-level information of CO_2 binding in the M_2(dbodc) family and studied how the identity of the metal cation effects the local structure around CO_2 adsorption sites and the CO_2 adsorption properties. This experimental work has further allowed us to make a detailed comparison with state of the art DFT calculations. Our combined synthetic, characterization, and computational effort renders unique insights into the molecular aspects of CO_2 adsorption in these materials, and this understanding will help us accelerate the search for materials with the properties needed for a range of important gas separations.[38,39]

Experimental

Synthesis

The compounds M_2(dobdc) (where M = Mg, Mn, Fe, Co, Ni, and Zn) were synthesized using slight modifications to previously published procedures.[40,41] For Mg, Mn, Co, Ni, and Zn, the reaction mixtures were sparged with argon for 1 h prior to heating. All MOF reactions were halted after 18 h, after which solvent exchanges were performed as described elsewhere.[42]

Attempts to reproduce the previously published procedure for synthesizing Cu_2(dobdc) afforded an impure material,[43] as determined by X-ray powder diffraction. The following procedure was therefore developed for synthesizing pure Cu_2(dobdc). Into a 20 mL glass scintillation vial were added H_4dobdc (29.7 mg, 0.150 mmol), $Cu(NO_3)_2 \cdot 6H_2O$ (111 mg, 0.375 mmol), and 10 mL of a mixed solvent (60 : 40 iPrOH : DMF). The solution was sparged with argon and the vial was sealed with a Teflon-lined cap and placed in a 2 cm deep well plate on a 373 K hot plate. After 45 min a black powder formed on the bottom and walls of the vial. Longer reaction times produced a green solid impurity. The reaction mixture was then decanted and the remaining powder was soaked in 20 mL of DMF at 343 K for 12 h, after which the solvent was decanted and replaced with fresh DMF. This process was repeated 6 times over the course of 3 days after which the solvent was switched to methanol and the process was repeated. The solid was then collected by rapid filtration and fully desolvated by heating under dynamic vacuum (<10 μbar) at 523 K for 24 h to afford 22.5 mg (47%) of Cu_2(dobdc) as a black microcrystalline solid.

Deuteration of 2,5-dihydroxy-1,4-benzendicarboxylic acid took place at the National Deuteration Facility, Lucas Heights, Australia. A mixture of 2,5-dihydroxy-1,4-benzenedicarboxylic acid (2.5 g, 12.6 mmol), Pt/activated carbon (2.5 g, 10 wt% of the substrate, 1.28 mmol Pt) and 40% w/w NaOD (6 g, 146.3 mmol) in D_2O (120 mL) was loaded into a Parr pressure reactor (600 mL size). The contents of the reactor were degassed by purging with N_2 gas, followed by a purge with an atmosphere of H_2 gas, and then sealed and heated to 180 °C, with constant stirring for 1 day. The reactor was cooled to room temperature, and the contents were filtered through a short plug of Celite, to remove the catalyst, which was further washed with ice water (100 mL). The aqueous filtrate was acidified using 1 M HCl that changed the color of the mixture from a clear orange solution to bright yellow with a fine suspension that was collected by filtration. Thin layer chromatography was used (referenced with the protonated compound) to estimate the purity and to develop separation protocols. ^{1}H NMR (400 MHz) and ^{2}H NMR (61.4 MHz) spectra were recorded on a Bruker 400 MHz spectrometer at 298 K. The collected yellow solid was dissolved in an ethyl acetate and methanol mixture (7 : 3 ratio) and loaded on a short silica column prepared in the same solvent mixture. A small amount of impurity was isolated first by eluting the column with the solvent mixture, and then the product was collected using increasing ratios of methanol to ethyl acetate. The pure fractions were isolated and subjected to high vacuum to give 2,5-dihydroxy-1,4-benzenedicarboxylic-d_2 (dobdc-d_2) (1.8 g, 72% yield, ≥98% D by NMR and MS). ^{1}H NMR (400 MHz, acetone-d_6): δ_H 7.43 (s, residual 2 × Ph-H). ^{2}H NMR (61.4 MHz, acetone-d_6): δ_D 7.46 (bs, 2 × Ph-D). $^{13}C\{^1H\}$ NMR (100.6 MHz, $CDCl_3$) δ_C 117.3 (t, 2 × Ph-D), 118.4 (s, qC), 153.1 (s, qC), 170.5 (s, COOH). $^{13}C\{^1H,^2H\}$ NMR (100.6 MHz, $CDCl_3$, D1 = 20 s) δ_C 117.3 (s, 2 × Ph-D, integration 1), 117.6 (s, residual 2 × Ph-H, integration 0.02), 118.4 (s, qC), 153.1 (s, qC), 170.5 (s, COOH). ESI-MS (negative mode) (deuterated, M_w = 200) showed two signals at m/z 199 (M^{-1}) and 198 (M^{-2}) while protonated version of 2,5-dihydroxy-1,4-benzenedicarboxylic (protonated, M_w = 198) showed two signals at m/z 197 (M^{-1}) and 196 (M^{-2}) (Fig. S1–S4†). See ESI† for chemical information. Mg_2(dobdc-d_2) was synthesized from the as-prepared dobdc-d_2 ligand for use in INS studies.

CO_2 adsorption and surface area measurements

For gas adsorption isotherms, UHP-grade (99.999% purity) helium, nitrogen, and carbon dioxide were used for all measurements at pressures ranging from 0 to 1.1 bar using a Micromeritics ASAP 2020 instrument.§ Samples were first transferred under a N_2 atmosphere to preweighed analysis tubes, which were capped with a Transeal. The samples were evacuated on the ASAP until the outgas rate was less than 3 μbar min^1. The evacuated analysis tubes and samples were then carefully transferred to an electronic balance and weighed to determine the mass of sample (typically 100–200 mg). For cryogenic measurements, the tube was fitted with an isothermal jacket and transferred back to the analysis port of the gas adsorption instrument. The outgas rate was again confirmed to be less than 3 μbar min^{-1}. Langmuir surface areas and pore volumes were determined by measuring N_2 adsorption isotherms in a 77 K liquid N_2 bath and calculated using the Micromeritics software, assuming a value of 16.2 Å^2 for the molecular cross-sectional area of N_2. Adsorption isotherms between 25 and 45 °C were measured using a recirculating dewar (Micromeritics) connected to a Julabo F32-MC isothermal bath (Fig. S5–S13 and Tables S1–S7†).

Single crystal and powder diffraction

High resolution neutron powder diffraction (NPD) experiments (for M_2(dobdc), M = Mg, Mn, Co, Cu, or Zn) were carried out using BT1 at the National Institute of Standards and Technology Center for Neutron Research (NCNR) or (for M = Fe) using Echidna[44] at the Bragg Institute within the Australian Nuclear Science and Technology Organisation (ANSTO). All measurements were carried out on activated samples ranging from 0.8 to 1.5 g. At NIST, samples were activated while heating under dynamic vacuum and then transferred into a He purged glovebox, loaded into a vanadium can equipped with a gas loading valve, and sealed using an indium O-ring. NPD data were collected using a Ge(311) monochromator with an in-pile 60° collimator corresponding to a wavelength of 2.0782 Å. The samples were loaded onto a closed cycle refrigerator (CCR) and then data were collected at 10 K. After data collection of the bare material, CO_2 loading was then carried out. The sample was warmed to room temperature and then exposed to a predetermined amount of gas. Upon reaching an equilibrium pressure at the loading temperature, the sample was then slowly cooled (1 K min^{-1}) to ensure complete adsorption of the CO_2. Data was then collected again at 10 K. At ANSTO, a desolvated sample of Fe_2(dobdc) weighing 1.079 g was transferred to a vanadium cell equipped with a gas line and heaters inside of an Ar-filled glovebox. The high-resolution diffractometer was configured with a Ge(331) monochromator using a takeoff angle of 140° with no collimation at the monochromator and fixed tertiary 5′ collimation, resulting in a wavelength of 2.4406 Å. NPD data were collected at approximately 9 K for the evacuated framework and then subsequently heated to room temperature, dosed with 0.5 CO_2 and 1.5 CO_2/Fe^{2+}, and then slowly recooled again to 10 K where data was recollected. It should be noted, that the same samples were utilized for both gas adsorption measurements and for structural studies (Fig. S14–S19 and Tables S8–S23†).

Additional NPD measurements of CO_2-loaded Fe_2(dobdc) were performed on the high-intensity neutron powder diffractometer, WOMBAT,[45] also located at the Bragg Institute at ANSTO. The WOMBAT instrument was configured with a Ge(113) monochromator with a take-off angle of 110° with open primary and secondary collimation, resulting in a wavelength of 2.7948 Å. Data were collected at select temperatures upon cooling. Temperatures ranged between 10 and 300 K for the bare Fe_2(dobdc) framework and then again with sequential loadings of 0.5 CO_2 and 1.5 CO_2 molecules per iron. For each loading, the cryostat and sample were heated to 300 K to dose CO_2 gas (Fig. S22 and S23†).

All NPD data were analyzed using the Rietveld method as implemented in EXPGUI/GSAS.[46,47] The activated M_2(dobdc) model was refined with most structural and peak profile parameters free to vary, resulting in a structure very similar to that determined using single crystal X-ray diffraction. Atomic displacement parameters (ADPs) for atoms with the same identity were constrained to be the same throughout the refinement process. Fourier difference analysis, applied to data obtained from CO_2 adsorbed samples, was then employed to locate the adsorbed molecules in the frameworks. With the exception of the Fe and Mg analogs, intramolecular bond distances and angles of the adsorbed molecules were initially restrained to values expected for a free CO_2 molecule. Once refinements became stable, the values were allowed to vary freely. The modeled atoms within each CO_2 molecule were constrained to maintain the same fractional occupancies throughout the refinement. For analysis of the large number of lower resolution data sets collected on WOMBAT, sequential refinements were carried out using the GSAS/EXPGUI[46,47] software package. First, Rietveld refinement of a single data set was carried out manually and then the parameters obtained from the first data set were used as a starting point for the subsequent and automatic refinement of the remaining data sets.

In an attempt to elucidate the global minimum structure for CO_2 in Cu_2(dobdc), data was collected at 100 K on the XSD rapid-acquisition powder beamline, 17-BM-B, at the Advanced Photon Source (APS) at Argonne National Laboratory. Desolvated Cu_2(dobdc) with a mass of approximately 9 mg was loaded into a quartz capillary in a N_2-purged glove box. The capillary was attached to a custom gas-dosing cell equipped with a gas valve. Cu_2(dobdc) was further activated *in situ* by heating the capillary at 380 K for 1.5 h under dynamic vacuum provided *via* a turbomolecular pump. The samples was cooled to room temperature, dosed with approximately 1.5 CO_2 per Cu^{2+}, and slowly cooled to 100 K for data collection. 17-BM-B has an incident energy range of 15–18 keV and calibrated cycle wavelength of 0.72959 Å (Fig. S31 and Table S26†).

For single crystal structural analysis, a methanol solvated crystal of Co_2(dobdc) was mounted on a Kapton loop using a minimal amount of epoxy applied only on faces that propagate in directions parallel to the channel direction (along the long axis of the rod-shaped crystals). The sample was then placed in a custom-made gas cell equipped with a gas loading valve and a borosilicate glass cap sealed with an O-ring. The cell was evacuated under reduced pressure at 473 K for 4 h to remove solvent molecules. Data was then collected at Beamline 11.3.1 at the Advanced Light Source, Lawrence Berkeley National Laboratory using synchrotron radiation ($\lambda = 0.77490$ Å). A Bruker AXS APEX II diffractometer was used for data collection, and the corresponding Bruker AXS APEX II software was used for data collection and reduction.[48] The structure of the desolvated crystal was obtained from a preliminary data set to confirm the absence of solvent bound at the Co sites. The cell was then warmed to room temperature and dosed with 6.7 mbar of CO_2. The cell was subsequently cooled at a rate of 2 K min^{-1} to a final temperature of 150 K. The crystal was found to be an obverse/reverse twin based on the diffraction pattern. The program CELL_NOW was used to determine the orientation matrices and the domains were found to be related by a 180° rotation around the reciprocal axis [0 1 1].[49] Raw data for both matrices were integrated and corrected for adsorption using TWINABS.[50] The structure was solved using direct methods with SHELXS[51,52] and refined using SHELXL[51,52] operated in the OLEX2 interface.[53] ADPs were refined anisotropically for all non-hydrogen atoms. Hydrogen atoms were placed in ideal positions and refined using a riding model. Site occupancy factors for CO_2 bound to Co and at a secondary site were refined using two separate independent free variables. Disorder of the two CO_2 molecules in the structure required the use of restraints during structure refinement. Additional electron density that could not be modeled was found inside the pore, which is likely due to additional CO_2 that is severely disordered (Tables S24, S25 and Fig. S20†).

Inelastic neutron scattering

Inelastic neutron scattering (INS) experiments were performed on 0.7057 g of Fe_2(dobdc) employing the Filter Analyzer Neutron Spectrometer (FANS) at the NCNR.[54] Spectra were obtained by illuminating the samples with a collimated and monochromated neutron beam. After passing through a low-energy band-pass filter consisting of Bi, Be, and graphite, the energy transfer of the scattered neutrons was determined at a bank of ^{3}He detectors. Data were first collected for the bare framework, followed by data collection for the framework loaded with 0.75 CO_2 per Fe. Gas was loaded into the framework using the same methods as described for the high-resolution NPD experiments. The spectra of the bare framework were then subtracted from the spectra obtained for the CO_2 loaded sample using the DAVE suite of programs (Fig. S24†).[55] This process was repeated on 0.834 g of Mg_2(dobdc-d_2) using the TOSCA spectrometer at ISIS.

Density functional theory calculations

To study CO_2 adsorption in M_2(dobdc) systems from first principles, we used density functional theory (DFT) within the generalized gradient approximation of Perdew, Burke, and Ernzerhof (PBE)[56] and a van der Waals dispersion-corrected functional (vdW-DF2).[57] The VASP program package[58] with a planewave basis set and projector augmented wave[59] pseudopotentials was used for all calculations. A Hubbard-like U parameter[60] was employed to better treat the localized d-states of the transition metal cations. We used an energy cutoff of 1000 eV for the planewave basis set and Brillouin zone sampling at the Γ-point, leading to binding energies that converged to within 1 kJ mol^{-1}. Previous works have studied CO_2 adsorption in M_2(dobdc) systems at a variety of levels of theory,[61–67] although typically the focus of these studies has been confined to some subset of the systems investigated here[61–65] or has not been directed towards binding geometries.[61,65,66] We find reasonable quantitative agreement between our data and the only previous study addressing geometries and encompassing all M_2(dobdc) systems studied here.[67]

To generate binding geometries, we first optimized periodic M_2(dobdc) crystals in a triclinic primitive unit cell of 54 atoms

using PBE + U, beginning from the experimental Zn_2(dobdc) structure and substituting in other divalent metal cations (Mg, Mn, Fe, Co, Ni, and Cu) at all metal sites, until the residual forces were smaller than 0.01 eV $Å^{-1}$ and the stress tensor components were smaller than 0.2 kbar. The computed lattice parameters are all within 2% of experiment. For open-shell cations, we employed Hubbard-like U corrections. Values of U used were 4.0, 4.0, 3.3, 6.4, and 4.0 eV for Mn, Fe, Co, Ni, and Cu, respectively; these values were taken from ref. 68, where they were determined for each metal cation to reproduce the experimental oxidation energy of MO to M_2O_3. For all M_2(dobdc) analogs, we find a high-spin ground state, and we assumed ferromagnetic ordering along the metal-oxide chain direction and antiferromagnetic ordering between the chains, as observed for the ground state magnetic ordering in Fe_2(dobdc).[69] To predict adsorption geometries, CO_2 was relaxed inside rigid periodic M_2(dobdc) frameworks using vdW-DF2 + U at a loading of one molecule per six metal sites. vdW-DF2 was shown in previous work to provide excellent binding energetics for CO_2 adsorption to M_2(dobdc) systems.[64] vdW-DF2 + U was also used in single-point calculations to compute the energies of the bare M_2(dobdc) frameworks for use in calculating binding enthalpies.

Binding enthalpies at 308 K were calculated by including quantum zero-point energies (ZPEs) and finite-temperature thermal energies (TEs) at the level of a harmonic approximation. The enthalpy of adsorption of a molecule in a MOF is calculated as:

$$-\Delta H(T) = H(T)(\mathrm{CO_2} + \mathrm{MOF}) - H(T)(\mathrm{CO_2}) - H(T)(\mathrm{MOF}),$$

where $H(T)$(MOF), $H(T)$(CO_2), and $H(T)$(CO_2 + MOF) are the enthalpies (at temperature T) of the bare MOF without CO_2, CO_2 in the gas phase, and the MOF with CO_2 adsorbed, respectively.

Results and discussion

CO_2 adsorption properties

Low-pressure CO_2 adsorption isotherms were collected for Fe_2(dobdc) at 298, 308, and 318 K, as shown in Fig. 2. The steep initial rise in CO_2 uptake, likely due to strongly polarizing adsorption sites, is a feature often observed in the presence of coordinatively-unsaturated metal centers. The adsorption capacity at 1.1 bar and 298 K of 7.2 mmol g^{-1} corresponds to a value slightly higher than expected for 1 CO_2 per iron(II) site and implies additional contributions from secondary adsorption sites. The isosteric heat ($-Q_{st}$) of CO_2 adsorption was calculated by fitting the adsorption isotherms at each temperature with a dual-site Langmuir–Freundlich equation (see ESI† for details). At a loading of 0.1 CO_2 per iron(II), the heat of adsorption was determined to be 33.2(1) kJ mol^{-1}, as shown in the inset of Fig. 2. This value is significantly smaller than that reported for Mg_2(dobdc),[34] which is expected when considering the softer nature of the iron(II) cation (ionic radii for Fe^{2+} = 0.74 pm, Mg^{2+} = 0.66 pm) and electrostatic nature of the adsorbate/adsorbent interaction. These observations are supported quantitatively by our DFT calculations, which predict heats of adsorption (at 298 K) of 34.1 and 40.9 kJ mol^{-1} for Fe_2(dobdc) and Mg_2(dobdc), respectively, at a loading of 1 CO_2 per 6 metal cations.

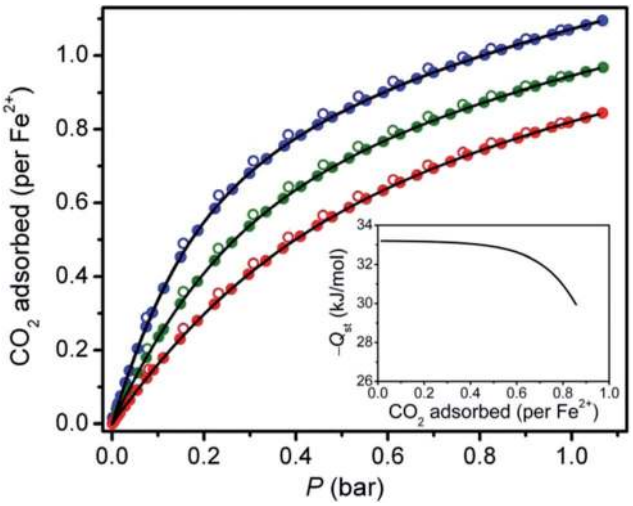

Fig. 2 Excess CO_2 adsorption isotherms collected for Fe_2(dobdc) at 298 K (blue), 308 K (green), and 318 K (red). Filled and open circles represent adsorption and desorption, respectively. The solid black lines correspond to dual-site Langmuir–Freundlich fits to the CO_2 adsorption isotherms. Inset: isosteric heat of adsorption ($-Q_{st}$) plotted as a function of adsorbed CO_2.

To correlate structure with CO_2 adsorption properties for this isostructural series, Mg-, Mn-, Co-, Ni-, Cu-, and Zn-frameworks were synthesized and characterized in addition to Fe_2(dobdc). While the CO_2 adsorption properties of many of these materials have been previously reported,[16,34–36,67,70,71] there are some inconsistencies, likely due to variations in synthetic procedures and/or sample activation or handling, making it difficult to assess the accuracy of some reported results.[71] Fig. 3a shows the adsorption isotherms obtained for the seven analogues in the M_2(dobdc) series at 298 K. The data is plotted as mol CO_2/mol M^{2+} rather than the typical units of mmol CO_2/g sample to avoid the effects of slight variations in formula weight. In the low-pressure regime, there is a notable difference in the CO_2 adsorption properties, indicating that the open metal site dominates the adsorption process. Although binding strengths at the primary adsorption site vary throughout the series, upon saturation of the metals at higher pressures or lower temperatures, it is expected that the isotherms will begin to resemble one another due to the isostructural nature of the frameworks. Indeed, approaching 1 bar, the capacity of the Mg, Ni, Fe, and Co frameworks are already very similar with ~1.1 CO_2 per metal(II) indicating that these materials are already approaching the saturation capacity of the primary adsorption site.

After fitting each isotherm with a dual-site Langmuir–Freundlich equation, the isosteric heats of CO_2 adsorption were calculated for each framework and show the following trend at a loading of 0.1 CO_2 per M^{2+}: Mg > Ni > Co > Fe > Mn > Zn >Cu (Fig. 3b), with $-Q_{st}$ values that range from 22.1(2) to 43.5(2) kJ mol^{-1} (Table 1). In good agreement with experimentally determined heats of adsorption, DFT calculations show binding

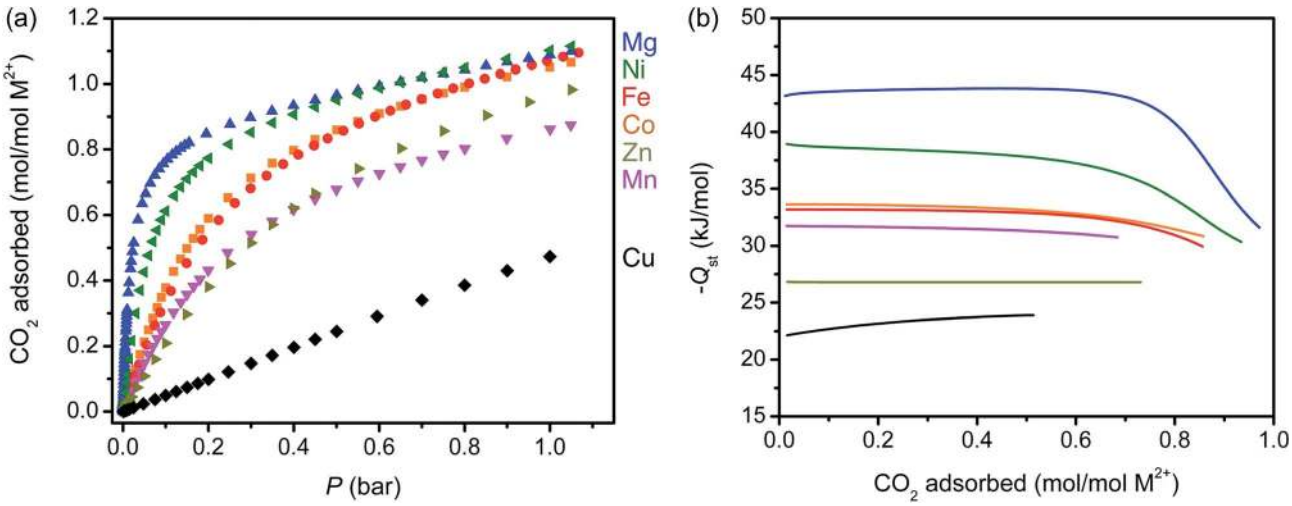

Fig. 3 (a) Excess CO_2 adsorption isotherms collected for the M_2(dobdc) series at 298 K. (b) Low coverage $-Q_{st}$ for the M_2(dobdc) series determined from CO_2 adsorption isotherms collected at 298, 308, and 318 K. The color scheme is the same for both images.

enthalpies, $-\Delta H$, that range from 27.1 to 40.9 kJ mol^{-1} at 0.167 CO_2 per M^{2+}. While the theoretically determined trend, Mg > Ni > Fe > Mn > Co > Zn > Cu, is slightly different from the experimental one, these differences are only observed for intermediate adsorbents including Mn, Fe, and Co, which exhibit similarities in CO_2 binding strength. A full comparison of our experimental data and the DFT results is provided in Table 1.

Based on the electrostatic nature of the interaction between the M^{2+} cations and CO_2, one might expect that the observed trend should follow that of the ionic radii, as it does in a series of M-BTT MOFs;[72] however, significant deviations are observed. A recent report by Yu *et al.*[67] gives an explanation for the observed trend through a description of nuclear screening effects by M^{2+} d-orbitals. Their first-principles study reveals that the relative strength of the electrostatic interaction is dictated by the effective charge of the metal cations at the open coordination site where CO_2 binds. The isosteric heats of adsorption are fairly continuous for Mn, Zn, and Cu, while the $-Q_{st}$ for Mg and Ni show an abrupt change between 0.7 and 0.8 CO_2 per M^{2+} (Fig. 3b), possibly implying that not all of the metal sites are accessible. This discontinuity also implies that there is a significant difference in energetics associated with the primary and secondary adsorption sites of the strongly adsorbing frameworks. Further, as the coverage approaches 1 CO_2 per M^{2+} for Mg, Ni, Co, and Fe, the isosteric heats approach a similar value of ~32 kJ mol^{-1}, indicative of a homogenous distribution of adsorption enthalpies of the secondary adsorption sites, a direct result of the similar adsorption environments across the isostructural series.

Structural studies with low CO_2 coverage

In order to study the structural characteristics of the framework as a function of CO_2 loading, detailed powder diffraction experiments (10 K) were carried out on Fe_2(dobdc) using a high-resolution neutron diffractometer. Analysis of data obtained from the bare framework revealed no excess scattering density

Table 1 Experimental and theoretical (DFT) data comparing CO_2 adsorption properties of the M_2(dobdc) series[a,b]

	M···O(CO_2) (Å)		∠O–C–O(CO_2) (°)		∠M–O–C(CO_2) (°)		$-Q_{st}$[c] (kJ mol^{-1})	$-\Delta H$[d] (kJ mol^{-1})
M	Experiment	Theory	Experiment	Theory	Experiment	Theory	Experiment	Theory
Mg	2.27(1)	2.41	178(2)	178.3	131(1)	123.8	43.5(2)	40.9
Mn	2.51(3)	2.57	176(3)	178.8	120(2)	122.2	31.7(1)	33.9
Fe	2.29(3)	2.62	179(3)	178.7	106(2)	120.6	33.2(1)	34.1
Co	2.23(4)	2.56	174(4)	178.7	118(2)	118.6	33.6(1)	33.8
Co	2.261(9)[e]	2.56	171(6)[e]	178.7	133(3)[e]	118.6	—	33.8
Ni	2.29(3)[f]	2.52	162(3)[f]	178.6	117(2)[f]	120.1	38.6(6)	37.3
Cu	2.86(3)	2.87	180(2)	179.1	117(1)	112.4	22.1(2)	27.1
Zn	2.43(4)	2.84	178(6)	178.7	117(3)	114.6	26.8(1)	30.2

[a] Values reported came from this study unless otherwise specified. [b] Structural parameters from neutron diffraction data were obtained from CO_2 loadings ranging from 0.35 to 0.82 CO_2 per M^{2+} at 10 K (see ESI† for further details). [c] Low-coverage CO_2 isosteric heats of adsorption for the M_2(dobdc) analogues were calculated at a loading of 0.1 CO_2 per M^{2+}. [d] Theoretical values were calculated using 0 K DFT binding enthalpies corrected at the harmonic level for ZPE and TE contributions, at loadings of 0.167 CO_2 per M^{2+}. DFT binding energies on which these binding enthalpy calculations are based have been previously published in ref. 72. [e] Values were obtained from single crystal X-ray diffraction at 150 K and a loading of 1.5 CO_2 per Co^{2+}. [f] Values were previously reported by Dietzel *et al.* in ref. 74.

in the channels, indicating that the materials were completely activated. Rietveld refinement of the host framework, followed by Fourier difference analysis allowed the subsequent elucidation of CO_2 site positions and occupancies. The material was first loaded with 0.5 CO_2 per iron(II) site at room temperature. After slowly cooling, the adsorption of CO_2 was less than was initially loaded, 0.350(6) CO_2 per iron(II), due to a small fraction of CO_2 freezing in the gas line of the top-loading CCR. Comparing the bare framework to that of the first loading reveals a decrease in unit cell volume from 4041.3(1) $Å^3$ to 4021.4(2) $Å^3$, which results from compression of the *a* and *b* axes upon adsorption (Fig. 4). The overall reduction in unit cell volume is 0.5%, a value that is slightly less than that previously reported for the CO_2-loaded Mg analog.[73] At this low-loading, there is population of a single site, site I, that is in close proximity to the iron(II) center, revealing that the open metal site is indeed responsible for the high initial isosteric heat of CO_2 adsorption (Fig. 5). The adsorbed CO_2 has an angular orientation with respect to the framework surface, with an M–O–C angle of 106(2)°, a direct result of weak, secondary van der Waals interactions with the framework ligand. The observed Fe^{2+}–O(CO_2) distance is 2.29(3) Å, a value that, within error of the experiment, is similar to those observed for the Mg and Ni analogs.[73,74]

Increasing the CO_2 loading in Fe_2(dobdc) from 0.35 to 1.3 CO_2 per iron(II) leads to an increase in site I occupancy as well as population of a secondary adsorption site (Fig. 5). The site II CO_2 molecule is nearly orthogonal to site I and lies almost parallel to the framework surface. Both sites I and II are surrounded by three nearest neighbouring CO_2 molecules exhibiting weak van der Waals type interactions, as indicated by long intermolecular distances that average around 2.8 Å (drawn as blue dashed lines in Fig. 6). Distances between site II CO_2 and the framework are all slightly above 3 Å, implying that the intermolecular interactions are likely aiding in the stabilization of the population of site II. Further, the population of site II is facilitated by an increase in the M–O–C angle from 106(2)° to 117.2(8)°, while there is little change in the M–O(CO_2) distance, from 2.29(3) Å to 2.27(1) Å. The observed change in the M–O–C angle, which is also supported by NMR experiments performed on CO_2 adsorbed Mg_2(dobdc) by Kong *et al.*,[75] might suggest

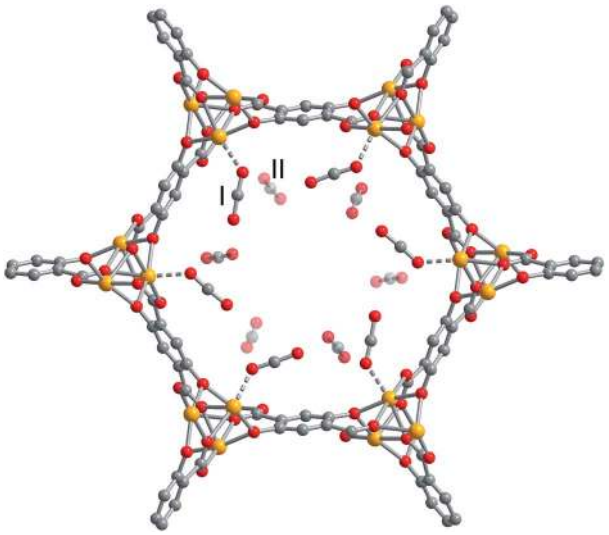

Fig. 5 Ball and stick model showing a single channel in Fe_2(dobdc) that is loaded with 1.5 CO_2 per iron(II) site. From the NPD data, there are two apparent CO_2 sites labeled as I and II in order of binding strength. Site II is drawn transparent to represent the 40% CO_2 occupancy. Orange, grey, and red spheres represent Fe, C, and O atoms, respectively; H atoms are omitted for clarity.

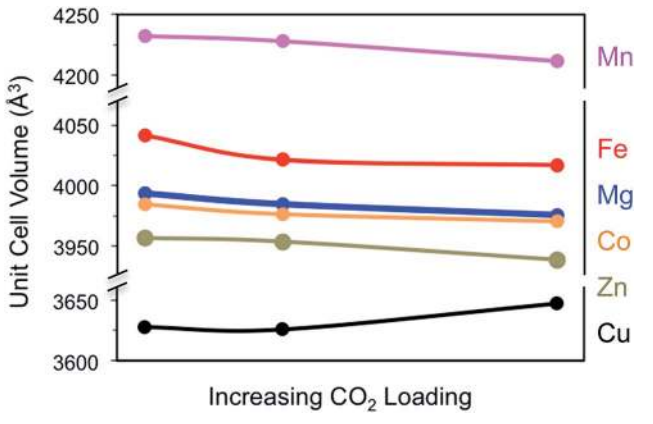

Fig. 4 Unit cell volumes plotted as a function of increased CO_2 loading. The first point represents the bare structure, the second point represents an intermediate CO_2 loading that ranges from 0.3 CO_2 to 0.6 CO_2 per open metal, and the last represents CO_2 loadings ranging from 1.3 to 1.8 CO_2 per metal(II). Error bars in all cases are smaller than the symbol and represent a single standard deviation. Mg data (blue) was included from ref. 73. All data are powder neutron diffraction and were collected at 10 K except for the highest loading of Cu_2(dobdc), which was included from 120 K powder X-ray diffraction (black).

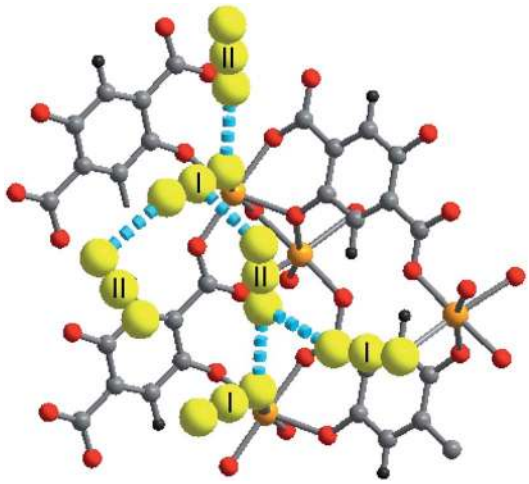

Fig. 6 Ball and stick model of site I and II CO_2 molecules (each represented as three yellow spheres) lining the framework wall of Fe_2(dobdc). Site I and II occupancies are 0.856(6) and 0.407(6), respectively. It should be noted that sphere size does not accurately represent ADPs. Nearest neighbor intermolecular interactions are drawn with blue dashed lines. Orange, grey, red, and black spheres represent Fe, C, O, and H atoms, respectively.

that, while there is minimal consequence on the electrostatic interaction between Fe^{2+} and CO_2, maximizing the van der Waals contacts for site II is necessary for realizing population of the weaker adsorption site. After full population of the secondary adsorption site, it is expected that further CO_2 adsorption will occur in the channels away from the framework walls, as there appears to be no room remaining on the surface for population of a tertiary adsorption site, as demonstrated in the space filling model shown in Fig. S25.†

High-resolution NPD data were also collected for several other isostructural analogs, including Mg-, Mn-, Co-, Cu-, and Zn_2(dobdc). Data were first collected on the bare frameworks, and then with CO_2 loadings ranging from 0.5 to 1.5 CO_2 per metal(II). The aforementioned issues with CO_2 freezing in the gas line were alleviated through the design of a custom-made gas-loading collar that fit securely to a bottom-loading CCR.

Diffraction data collected on the Cu analog was used to assess the extremely low enthalpy of CO_2 adsorption, nearly linear CO_2 uptake, and significantly lower CO_2 capacity at 1 bar (Fig. 3). Data from the bare framework reveals no excess scattering density in the channels, indicating that the material has been fully activated; however, the local environment around the Cu^{2+} cation is highly distorted. An axial elongation (Jahn–Teller-like) results in a Cu–O(1) bond of 2.441(8) Å, as compared to the average M–O(1) distance of 2.14 Å in the other M_2(dobdc) structures, and a slight twist in the metal bound carboxylate group that causes O(2) to point out away from the normal square planar arrangement of the equatorial O atoms and into the framework channel. These distortions are also captured in DFT calculations, which show a Cu–O(1) bond of 2.44 Å, as compared to an average M–O(1) distance of 2.16 Å for all experimentally studied M_2(dobdc) analogs. For comparison, a structural overlay of the MO_5 polyhedra obtained from analyses of NPD data is shown in Fig. S26.† A combination of this distortion and the overall lower effective ionic charge of the Cu^{2+} ion likely limits the approachability of the CO_2 molecule. Further, inefficient packing of CO_2 significantly limits the amount that can adsorb on the framework surface.

From *in situ* diffraction data collected on Cu_2(dobdc) loaded with 0.5 CO_2 per copper(II), three adsorption sites were identified (Fig. 7a). Two of these sites are located on the framework wall, while the tertiary site is found disordered inside the framework channel. Site I, found at the open metal, shows a significant elongation in the M–O(CO_2) distance of 2.86(3) Å, and a CO_2 coordination angle of 117(1)°. It should be noted that weak nuclear scattering density that results from weakly-bound/slightly-disordered CO_2 initially resulted in a local minimum for the structural analysis of this framework. This initial model showed CO_2 adsorption in a parallel orientation with the framework wall, rather than bound to the open metal site, (Fig. S27†). After further analysis a secondary adsorption site was identified that allowed stabilization of the expected model, with CO_2 adsorbed at the open metal (Fig. 7b). A comparison of the calculated diffraction pattern obtained from the structural model and the neutron diffraction data (Fig. 7c) reveals good agreement.

In addition to showing better agreement with the diffraction data, the new structural model also shows excellent agreement with the structural predictions from our DFT calculations (Fig. S28†). Further, a nudged elastic band[76] transition state method was used to further assess the potential existence of a kinetic barrier that might inhibit immediate adsorption at the open metal site and give rise to the existence of the initial structural model. The results show a monotonic decrease in energy (Fig. S29†), as the CO_2 moves from the less stable structure (Fig. S27†) to the more stable one (Fig. 7b), further indicating that no such barrier exists. As a last measure for further verification, high intensity X-ray diffraction data were additionally collected on CO_2 adsorbed Cu_2(dobdc) at the APS. The refined structural model further supports the final model obtained from NPD (Fig. S30 and Table S26†).

In previous studies, with other small molecules, such as D_2, we have shown that there is a direct correlation between isosteric heats of adsorption and metal–adsorbate distances.[77] However, this experiment reveals that Mg, Ni, Fe, and Co have the same M–O(CO_2) distances within the error of the

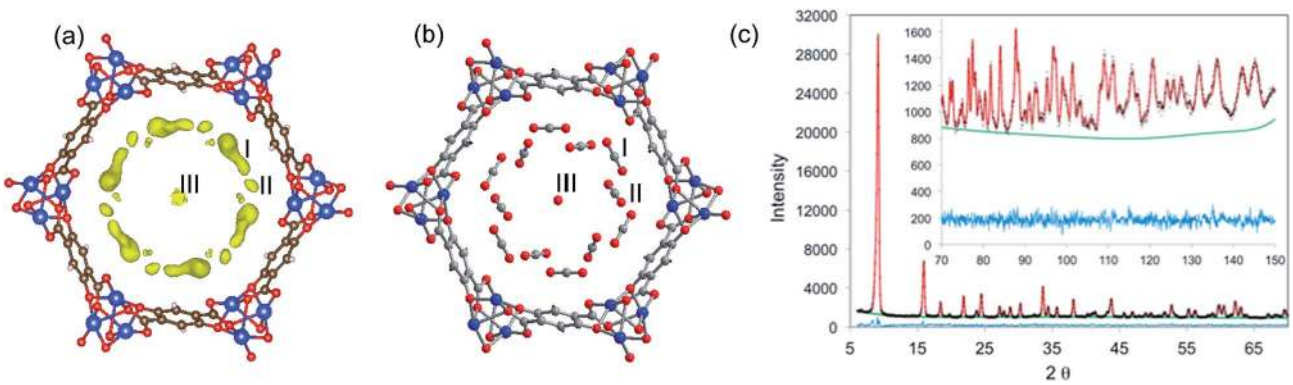

Fig. 7 (a) Fourier difference map revealing excess scattering density in Cu_2(dobdc) that results from CO_2 adsorption in the framework channel. The excess scattering for site II becomes more apparent with the inclusion of site I atoms in the model. (b) A ball and stick model of the finalized structure of Cu_2(dobdc) showing 3 CO_2 adsorption sites (determined from Rietveld analysis). (c) NPD data from Cu_2(dobdc) (10 K) after dosing with 0.5 CO_2 per Cu^{2+}. The green line, crosses, and red line represent the background, experimental, and calculated diffraction patterns, respectively. The blue line represents the difference between experimental and calculated patterns.

experiment (Table 1), despite significant variations in their $-Q_{st}$ values. It should be noted that the diffraction data were collected at 10 K, while the isosteric heats of CO_2 adsorption were calculated from isotherms collected at temperatures above 298 K. The difference in experimental conditions could result in slight variations in the local framework environment around CO_2 adsorption sites, leading to a difference in the observed correlations. However, Debye–Waller factors for room temperature powder diffraction data can significantly reduce the amount of structural detail extracted from the data if measured at higher temperatures. As such, most of the structural analysis reported here was carried out at low temperatures of ~10 K.

While the Mg-, Ni-, Fe-, and Co–O(CO_2) distances range from 2.23(4) Å to 2.29(3) Å, the Cu, Mn, and Zn analogs have elongated M–O(CO_2) distances of 2.86(3) Å, 2.51(3) Å, and 2.43(4) Å, respectively, which are in agreement with the lower isosteric heats of adsorption for the Cu-, Mn- and Zn-frameworks and the significantly larger ionic radius of Mn^{2+}. It should be noted that while angles between the site I CO_2 and the framework vary slightly from material to material, there is no correlation observed between strength of binding and the M–O–C angles, as was suggested in a previous report by Yu *et al.* Further, there is population of a similar secondary adsorption site for all materials within the series at higher loadings, with an increase in the M–O–C angle observed in each instance. However, there again is no observed correlation between the strength of binding and M–O–C angle. Our DFT calculations agree well with our experimental observations, as shown in Table 1. Our calculations corroborate the conclusion that the M–O–C angles do not necessarily correlate with increasing binding strength. Particularly, we see a deviation from this trend in Fe_2(dobdc) and Mn_2(dobdc), suggesting that M–O–C angle cannot necessarily be used to predict binding strength. Additionally, our measured and calculated M–O(CO_2) distances agree well relative to one another, with DFT consistently overestimating the distances, in line with the known behavior of vdW-DF2. The exception to this is Cu_2(dobdc), for which our experimentally measured and calculated M–O(CO_2) distances agree very well. The unexpected better agreement in this case is likely the consequence of secondary interactions with neighboring CO_2 molecules, which could induce an elongation in the Cu–O(CO_2) distance due to the overall weak interaction at the metal.

For the strongest CO_2 adsorbents, including Mg-, Ni-, Fe-, and Co_2(dobdc), no difference is observed in the M–O(CO_2) distances within error of the powder diffraction experiment. In order to see if a more highly resolved structural model could be obtained, additional single crystal studies were carried out on Co_2(dobdc), as this is the only compound in the series, other than Zn_2(dobdc), for which sizeable single crystals have been grown. Using a custom-designed gas cell and manifold, we dosed an activated single crystal with CO_2. The X-ray data collected at 150 K indicate a M–O(CO_2) distance of 2.261(9) Å and an angle of 171(6)° (Table 1). While the data do not show significant improvement in the refined CO_2 distances and angles, they do exhibit consistency with the values obtained from powder neutron diffraction at 10 K. For comparison, an overlay of the two structures is provided in Fig. S20.†

The O–C–O bond angle of adsorbed CO_2

The refined O–C–O angle of 179(3)° for Fe_2(dobdc) is within error of the expected linear geometry of a free CO_2 molecule, and, importantly, is significantly larger than previous reports for CO_2 adsorbed in the Mg and Ni analogs (164(6)° and 162(3)°, respectively), as obtained from both powder neutron[73] and X-ray diffraction.[74] Molecular bending has been of strong interest, as activation of the CO_2 molecule can indicate significant charge transfer between the adsorbed guest and framework, making strong implications towards chemical activation. However, bending could also result from significant static/dynamic disorder in the adsorbed CO_2 molecule that results in a misinterpretation of the bond angle from the time and position averaged diffraction experiments. Given the high-spin nature of the M^{2+} cations in M_2(dobdc), significant charge transfer is not expected and theoretical studies suggest that large deviations from the expected linear geometry will require a significant energy cost.[78] Further, dynamic disorder is not likely at the data collection temperature of 10 K. Therefore, it is expected that the large bending in previous reports is related to static disorder, an idea that is further supported by the large displacement parameters observed for the two CO_2 atoms that are not directly coordinated to the metal.[73] The refined CO_2 angle for Fe_2(dobdc) indicates that if there is activation of the adsorbed gas molecule, it cannot be seen within error of the powder diffraction experiment.

It should also be noted that the diffraction data obtained from the Fe_2(dobdc) (Fig. S16†), relative to the Mg_2(dobdc) previously studied, has much better data quality at higher angles or smaller *d*-spacings, from which more accurate structural detail can be determined. It is thought that a combination of cooling the sample slowly in the presence of CO_2 as a means of eliminating static disorder (1 K min^{-1}) and improving the crystallinity of the sample have significantly aided us in the accuracy of the refined angles, compared to those previously reported for the Ni and Mg frameworks.[73,74]

Given the stronger Mg–CO_2 interaction relative to Fe, we also varied the reaction conditions for the formation of Mg_2(dobdc) as a means to improve the crystallinity (Fig. S18†), and again slowly cooled the sample in the presence of CO_2. Here again, there is a significant improvement in the quality of the refined CO_2 angle for Mg_2(dobdc), 179(2)°, for a loading of 0.8 CO_2 per metal, a value that is for the first time much closer to those that have been predicted in this work (Table 1), and in previous DFT calculations.[64,67,78] This observation is supported both by our work and recent studies by Yu *et al.* and Poloni *et al.* who use several computational methods to predict that, while the CO_2 molecule is no longer linear, the intramolecular angle is at least larger than 174° upon adsorption in Mg_2(dobdc). This results from a largely electrostatic interaction between the metal cation of the framework and the adsorbed guest species.[64,67] It should be further noted that for all of the materials in this study there is limited bending observed in the metal-bound CO_2 with angles that range from 174(4)° to 180(2)° (Table 1).

Temperature-dependent structural studies

Diffraction data collected on a high flux neutron powder diffractometer allowed determination of the temperature-dependent properties of CO_2 adsorbed within Fe_2(dobdc) between 20 and 300 K (Fig. 8). The sample, loaded with 0.5 and then 1.5 CO_2 per iron(II), allowed a concerted evaluation of CO_2 adsorption level, as well as a determination of the site occupation. At a loading of 0.5 CO_2 per iron(II), there is population only at site I, without significant desorption occurring until ~200 K. If there is any population of site II during the heating process, it cannot be seen within the error of the experiment. For the 1.5 CO_2 per iron(II) loading, there is population of both sites with significant amounts of desorption again above 200 K. While there is minimal population of site II at room temperature, it should be noted that this occupancy is not zero, with a 5 : 1 ratio found for the population of sites I and II, respectively. The equilibrium pressure was monitored during the heating process (Fig. S22†), and at room temperature it was found to be 0.65 bar with the total population of sites I and II, equivalent to approximately 0.77 CO_2 per iron(II). The total CO_2 occupancy correlates well with the results obtained from the isotherm at 298 K, as shown in Fig. 3a.

Since the binding energy associated with adsorption at site II is thought to be somewhat similar across the series, it is expected that materials that bind CO_2 more strongly will exhibit a much larger contribution from site I CO_2 adsorption at low pressures and room temperature. For a qualitative comparison to the Fe analog, room-temperature neutron diffraction data were collected for Zn_2(dobdc). The data, collected at an equilibrium pressure around 0.65 bar, reveal an approximate 3 : 1 ratio for occupancies in site I and II, respectively, and a total occupancy of 0.62 CO_2 per zinc(II). The room temperature data collection reveals a slight elongation of the M–O(CO_2) distance and also a rearrangement of the secondary adsorption site that makes the intermolecular distances entirely too short for the two sites to be simultaneously occupied. Therefore, we consider that the overall weaker interaction at the open metal will not allow stabilization of the secondary adsorption site, and this directly correlates to less efficient packing of CO_2 molecules on the framework surface relative to the other analogs, except for Cu^{2+}. As in the case of Fe_2(dobdc), the refined CO_2 occupancy for Zn_2(dobdc) correlates well with that determined from the isotherms collected at 298 K (Fig. 3). In contrast to the room-temperature results for Fe and Zn, those previously obtained from Mg_2(dobdc) treated under similar conditions reveal no occupancy of site II within the error of the diffraction experiment and a nearly full occupancy of site I.[72] These results are not surprising, as occupation ratios are expected to increase with larger differences in binding energy of site I and II, as predicted by a Boltzmann distribution.

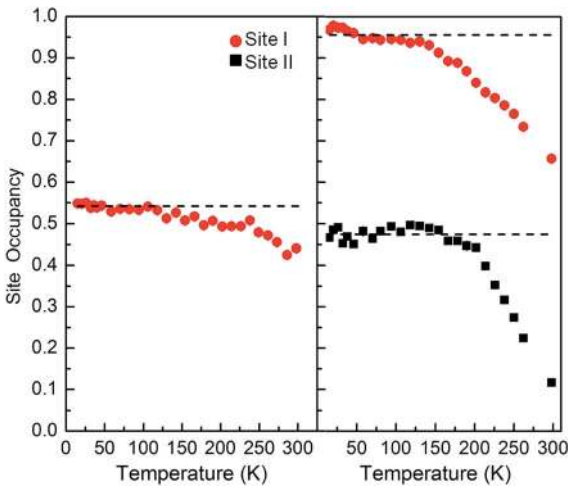

Fig. 8 Fe_2(dobdc) loaded with 0.5 CO_2 (left) and 1.5 CO_2 (right) per iron(II) site. The data were acquired using a high-intensity powder neutron diffractometer, WOMBAT. The red (site I) and black (site II) points are refined occupancies. The error bars, which are smaller than the symbols, represent a single standard deviation.

Inelastic neutron scattering

INS was used to probe the low-energy vibrational modes associated with adsorbed CO_2 molecules in Fe_2(dobdc) (Fig. S24†) using the FANS spectrometer. Data were first collected on the bare framework and then again with the sample loaded with 0.75 CO_2 per iron(II). A subtraction of the data (Fig. S24b†) collected for the bare sample was then performed to search for neutron energy loss related to vibrational or bending modes of the surface bound CO_2; however, the difference spectrum reveals negative and positive intensities, indicating significant shifts associated with the observed framework modes upon CO_2 adsorption. This is not surprising, as this framework exhibits a significant reduction in overall unit cell volume upon gas adsorption (Fig. 4), indicating that the bound CO_2 can easily perturb framework phonon frequencies. Both softening and hardening of the vibrational modes are observed, likely due to the inverse effect CO_2 adsorption has on the lengths of the *a*/*b*- and *c*-axes, as previously noted from the diffraction data.

Additionally, it is expected that the intensity related to vibrational modes of the CO_2 should be relatively weak compared to framework modes, since the incoherent scattering cross sections for C and O, relative to those of H, are weak. As a result, INS spectra were also collected for the Mg_2(dobdc-d_2) framework using the TOSCA spectrometer. The goal was to improve both the resolution of the spectra and achieve a lower contribution to the background spectrum from H atoms in the framework. However, despite deuteration of the framework ligand and the higher resolution instrument, there is still no convincing indication of vibrational modes associated with framework adsorbed CO_2 and no splitting of the CO_2 wag mode around 80 meV.

Surface areas

Langmuir surface areas of the six M_2(dobdc) compounds were determined through 77 K N_2 adsorption measurements (Fig. S6†). Comparisons made on a per gram basis (Table 2) immediately imply differences in the as-prepared materials. These problems are not resolved when taking variations in formula weight of the series into consideration, as the

Table 2 Surface areas in the M_2(dobdc) series

M_2(dobdc)	Langmuir SA (m^2 g^{-1})	SA ratio[a]	N_2 per unit cell (1 bar)
Mg	1957	0.87	42.6
Mn	1797	1	39.1
Fe	1536	0.86	43.2
Co	1438	0.82	41.3
Ni	1574	0.90	45.1
Cu	1515	0.90	43.4
Zn	1277	0.76	34.8

[a] Langmuir surface areas were first converted to m^2 mol^{-1} M_2(dobdc) basis to account for differences in formula weight and then divided by the molar surface area of Mn_2(dobdc) to obtain the surface area ratio.

normalized Langmuir surface area of Zn_2(dobdc) is still nearly 24% less than that of Mn_2(dobdc). Further, for all of the analogs including Mg, Mn, Fe, Co, Ni, and Cu, the number of N_2 per unit cell range from 39 to 45 N_2 at 1 bar, while Zn is significantly lower at 35 N_2 per unit cell. There has been some debate over reasons for the overall lower surface area associated with Zn_2(dobdc), relative to the other analogs.[16] Possible reasons could be related to any or a combination of the following: structural changes in the framework, the presence of an amorphous impurity, remaining ligand/solvent blocking the pores or open metal sites, or crystalline defects such as intergrowth that can block N_2 access to the channels.

The structural studies carried out here have been used to address some of these questions. Firstly, Fourier difference analysis of the diffraction data collected on the bare framework reveals no residual scattering density in the channels indicating that there is no remaining solvent at the open metal. Secondly, there is no evidence of a structural distortion around Zn or in the rest of the framework that might limit accessibility at low-temperatures (Fig. S21†). Thirdly, it is expected that the presence of an amorphous phase would inadvertently cause a disagreement in the amount of dosed CO_2 *versus* the refined CO_2 occupancy; however, Rietveld refinement of the 10 K diffraction data indicates that the CO_2 occupancies, 0.54(2) CO_2 per zinc(II), closely mirror the amount loaded, 0.5 CO_2, supporting the idea that there is likely no amorphous phase in this sample. Lastly, it might be attractive to draw correlations between the unit cell volumes of the activated M_2(dobdc) series with the determined surface areas. However, unit cell volumes reveal the following trend: Mn > Fe > Mg > Co > Zn > Cu (Fig. 4). The copper(II) analog is an outlier, exhibiting significantly lower cell volume relative to zinc(II) yet a high surface area; this result suggests that there is no correlation between these two variables and cannot be evaluated further without assessment of the structural characteristics of N_2 binding within the framework.

At higher CO_2 loadings, 1.5 CO_2 per zinc(II), the gas began condensing as the sample was cooled. The refined CO_2 occupancy in the 10 K data revealed a maximum achievable CO_2 loading of approximately 1.29 CO_2 per zinc(II), with a site I occupancy of approximately 0.69(2). This data indicates that a large fraction of open-metal sites, approximately 30%, are not accessed, as the sample has clearly reached a maximum capacity at a significantly lower loading than the other analogs. There are clearly fewer accessible metal sites in the compound, which could be the result of crystalline defects. However, Zn is one of the few analogs, with the exception of Co, for which we have thus far been successful in growing sizeable single crystals, implying that there might be some significant difference in the nucleation and growth processes relative to the other derivatives. A recent study has shown that the growth and nucleation rates for Zn are significantly larger than those of Co or Ni independent of the synthetic technique and that higher nucleation and growth rates have an inverse effect on pore volume.[79] When considering all of the information at hand, one cannot rule out that crystalline defects could give rise to lower surface areas and pose limitations on CO_2 adsorption.

Conclusions

The foregoing results reveal the first full experimental study of both the structural properties and gas adsorption behavior within an extensive isostructural series of MOFs of the type M_2(dobdc). Unlike previous studies, we show that intramolecular angles of CO_2 molecules adsorbed at the metal cations exhibit minimal deviations from 180°. This finding lends more awareness of the framework properties required to achieve CO_2 activation, information that is pertinent to ongoing discussions regarding chemical conversion of CO_2. Additionally, by computing binding structures and energetics using DFT, we have found excellent agreement with the experimental results. Powder neutron and single crystal X-ray diffraction data reveal minimal differences between the CO_2 adsorbed frameworks for M = Mg, Fe, or Co, despite significant differences in isosteric heats of CO_2 adsorption. Larger decreases in the strength of CO_2 binding at the open metal site leads to an elongated metal–O(CO_2) distance for Mn, Cu, and Zn. The Cu analog additionally reveals an axial elongation that also leads to a ligand oxygen atom positioned so as to inhibit the approach of CO_2 to the open metal site. Cu_2(dobdc) further has two adsorption sites of comparable binding strength, as evidenced by similarities in CO_2 site occupancy, even at 10 K. Assessment of room temperature diffraction and adsorption data reveals that a secondary adsorption site does contribute to the uptake properties of many of these materials.

This study has further drawn attention to possible crystalline defects associated with the M_2(dobdc) series. Both structural analysis and adsorption measurements indicate that for some of the analogs, in particular Zn, a large percentage of the open metal sites are inaccessible, an occurrence that likely stems from intergrowth and can seriously limit performance. As such, this study might warrant further investigation of crystallization processes within the whole series in order to understand correlations between reaction conditions and sample quality. It is our hope that in-depth experimental efforts like this one can provide the insight necessary for the eventual deliberate design of new materials for energetically favorable carbon capture technologies.

Acknowledgements

This research was supported by the U.S. Department of Energy, Office of Basic Energy Sciences, Division of Chemical Sciences, Geosciences and Biosciences under Award DE-FG02-12ER16362. Work at the Molecular Foundry was supported by the Office of Science, Office of Basic Energy Sciences, of the U.S. Department of Energy under Contract no. DE-AC02-05CH11231, and computational resources were provided by NERSC and LBNL Lawrencium. The contributions of E.D.B., J.A.M., M.I.G., D.G., J.D.H., K.L., B.S., J.B.N., and J.R.L. were further supported through the Center for Gas Separations Relevant to Clean Energy Technologies, an Energy Frontier Research Center funded by the U.S. Department of Energy, Office of Science, Office of Basic Energy Sciences under award DE-SC0001015. The Advanced Light Source is supported by the Director, Office of Science, Office of Basic Energy Sciences, of the U.S. Department of Energy under Contract no. DE-AC02-05CH11231. Use of the Advanced Photon Source, an Office of Science User Facility operated for the U.S. Department of Energy (DOE) Office of Science by Argonne National Laboratory, was supported by the U.S. DOE under Contract no. DE-AC02-06CH11357. Work at the National Deuteration Facility of ANSTO is partly funded by the National Collaborative Research Infrastructure Strategy. We like to thank A. J. "Timmy" Ramirez-Cuesta at ISIS for his help in carrying out the TOSCA measurements and Vanessa K. Peterson for her help carrying out the experiments on WOMBAT and Echidna at The Bragg Institute. We would further like to thank Greg Y. Morrison and James R. Nasiatka, of the Advanced Light Source for the design and fabrication of the gas-loading cell and dosing system used on Beamline 11.3.1 and Greg Halder for assistance with data collected at the XSD beamline 17-BM-B at the Advanced Photon Source, Argonne National Laboratory. We also thank NSF for providing graduate fellowship support for J. A. M., a Gerald K. Branch fellowship in chemistry for the support of E. D. B. and the NIST/NRC Fellowship Program for the support of M. R. H. Development of the gas cell and gas dosing manifold used at the Advanced Light Source was partially funded by the US Department of Energy (DOE), Office of Science, Office of Basic Energy Sciences under Award Number DE-SC0001015. We also acknowledge Professor O. M. Yaghi for the use of the D-8 Venture single crystal X-ray diffractometer at the Materials Science Division in LBNL.

Notes and references

§ Materials and equipment are identified in this paper only to specify adequately the experimental procedure. In no case does such identification imply recommendation by NIST nor does it imply that the material or equipment identified is necessarily the best available for this purpose.

1 *Statistical Review of World Energy 2004*, BP, http://www.bp.com.
2 *IPCC 5th Assessment Report: Climate Change 2014: Mitigation of Climate Change*, http://www.ipcc.ch.
3 B. Smit, J. R. Reimer, C. M. Oldenburg, and I. C. Bourg, *Introduction to Carbon Capture and Sequestration*, Imperial College Press, London, 2014.
4 K. Z. House, A. C. Baclig, M. Ranjan, E. A. van Nierop, J. Wilcox and H. J. Herzog, *Proc. Natl. Acad. Sci. U. S. A.*, 2011, **108**, 20428.
5 R. Socolow, M. Desmond, R. Aines, J. Blackstock, O. Bolland, T. Kaarsberg, N. Lewis, M. Mazzotti, A. Pfeffer, K. Sawyer, J. Siirola, B. Smit, and J. Wilcox, *Direct Air Capture of CO_2 with Chemicals: A Technology Assessment for the APS Panel on Public Affairs, American Physical Society*, 2011, http://www.aps.org/policy/reports/assessments/upload/dac2011.pdf.
6 D. M. D'Alessandro, B. Smit and J. R. Long, *Angew. Chem., Int. Ed.*, 2010, **49**, 6058–6082.
7 *CO_2 Emissions from Fuel Combustion*, International Energy Agency, Paris, 2010, http://www.iea.org.
8 A. L. Kohl and R. B. Nielsen, *Gas Purification*, Gulf Publishing Company, Houston, TX, 5th edn, 1997.
9 *Federal Efforts to Reduce Cost of Capturing and Storing Carbon Dioxide*, 2011, http://www.cbo.gov.
10 R. J. Kuppler, D. J. Timmons, Q.-R. Fang, J.-R. Li, T. A. Makal, M. D. Young, D. Yuan, D. Zhao, W. Zhuang and H.-C. Zhou, *Coord. Chem. Rev.*, 2009, **253**, 3042–3066.
11 J. Liu, P. K. Thallapally, B. P. McGrail, D. R. Brown and J. Liu, *Chem. Soc. Rev.*, 2012, **41**, 2308–2322.
12 E. D. Bloch, L. J. Murray, W. L. Queen, S. Chavan, S. N. Maximoff, J. P. Bigi, R. Krishna, V. K. Peterson, F. Grandjean, G. J. Long, B. Smit, S. Bordiga, C. M. Brown and J. R. Long, *J. Am. Chem. Soc.*, 2011, **133**, 14814–14822.
13 N. L. Rosi, J. Kim, M. Eddaoudi, B. Chen, M. O'Keeffe and O. M. Yaghi, *J. Am. Chem. Soc.*, 2005, **127**, 1504–1518.
14 P. D. C. Dietzel, Y. Morita, R. Blom and H. Fjellvåg, *Angew. Chem., Int. Ed.*, 2005, **44**, 6354–6358.
15 P. D. C. Dietzel, B. Panella, M. Hirscher, R. Blom and H. Fjellvåg, *Chem. Commun.*, 2006, **9**, 959–961.
16 S. R. Caskey, A. G. Wong-Foy and A. J. Matzger, *J. Am. Chem. Soc.*, 2008, **130**, 10870–10871.
17 W. Zhou, H. Wu and T. Yildirim, *J. Am. Chem. Soc.*, 2008, **130**, 15268–15269.
18 P. D. C. Dietzel, R. E. Johnsen, R. Blom and H. Fjellvåg, *Chem.–Eur. J.*, 2008, **14**, 2389–2397.
19 P. D. C. Dietzel, R. Blom and H. Fjellvåg, *Eur. J. Inorg. Chem.*, 2008, **23**, 3624–3632.
20 S. Bhattacharjee, J. S. Choi, S. T. Yang, S. B. Choi, J. Kim and W. S. Ahn, *J. Nanosci. Nanotechnol.*, 2010, **10**, 135–141.
21 M. Dincă, A. Dailly, Y. Liu, C. M. Brown, D. A. Neumann and J. R. Long, *J. Am. Chem. Soc.*, 2006, **128**, 16876–16883.
22 M. Dincă, W. S. Han, Y. Liu, A. Dailly, C. M. Brown and J. R. Long, *Angew. Chem., Int. Ed.*, 2007, **46**, 1419–1422.
23 K. Sumida, S. Horike, S. S. Kaye, Z. R. Herm, W. L. Queen, C. M. Brown, F. Grandjean, G. J. Long, A. Dailly and J. R. Long, *Chem. Sci.*, 2010, **1**, 184–191.
24 S. Biswas, M. Maes, A. Dhakshinamoorthy, M. Feyand, D. E. De Vos, H. Garcia and N. Stock, *J. Mater. Chem.*, 2012, **22**, 10200–10209.
25 S. S.-Y. Chui, S. M.-F. Lo, J. P. H. Charmant, A. G. Orpen and I. D. Williams, *Science*, 1999, **283**, 1148–1150.
26 M. Kramer, U. Schwarz and S. Kaskel, *J. Mater. Chem.*, 2006, **16**, 2245–2248.

27 L. J. Murray, M. Dincă, J. Yano, S. Chavan, S. Bordiga, C. M. Brown and J. R. Long, *J. Am. Chem. Soc.*, 2010, **132**, 7856–7857.
28 J. I. Feldblyum, M. Liu, D. W. Gidley and A. J. Matzger, *J. Am. Chem. Soc.*, 2011, **133**, 18257–18263.
29 O. Kozachuk, K. Yusenko, H. Noei, Y. Wang, S. Walleck, T. Glaser and R. A. Fischer, *Chem. Commun.*, 2011, **47**, 8509–8511.
30 Y. Liu, H. Kabbour, C. M. Brown, D. A. Neumann and C. C. Ahn, *Langmuir*, 2008, **24**, 4772–4777.
31 E. D. Bloch, W. L. Queen, R. Krishna, J. M. Zadrozny, C. M. Brown and J. R. Long, *Science*, 2012, **335**, 1606–1610.
32 S. Horike, M. Dincă, K. Tamaki and J. R. Long, *J. Am. Chem. Soc.*, 2008, **130**, 5854–5855.
33 Y.-S. Bae, C. Yeon Lee, K. C. Kim, O. K. Farha, P. Nickias, J. T. Hupp, S. B. T. Nguyen and R. Q. Snurr, *Angew. Chem., Int. Ed.*, 2012, **51**, 1857–1860.
34 D. Britt, H. Furukawa, B. Wang, T. G. Glover and O. M. Yaghi, *Proc. Natl. Acad. Sci. U. S. A.*, 2009, **106**, 20637–20640.
35 Z. R. Herm, J. A. Swisher, B. Smit, R. Krishna and J. R. Long, *J. Am. Chem. Soc.*, 2011, **133**, 5664–5667.
36 J. A. Mason, K. Sumida, Z. R. Herm, R. Krishna and J. R. Long, *Energy Environ. Sci.*, 2011, **4**, 3030–3040.
37 W. S. Drisdell, R. Poloni, T. M. McDonald, J. R. Long, B. Smit, J. B. Neaton, D. Prendergast and J. B. Kortright, *J. Am. Chem. Soc.*, 2013, **135**, 18183–18190.
38 L.-C. Lin, K. Lee, L. Gagliardi, J. B. Neaton and B. Smit, *J. Chem. Theory Comput.*, 2014, **10**, 1477–1488.
39 J. Kim, L.-C. Lin, K. Lee, J. B. Neaton and B. Smit, *J. Phys. Chem. C*, 2014, **118**, 2693–2701.
40 S. R. Caskey, A. G. Wong-Foy and A. J. Matzger, *J. Am. Chem. Soc.*, 2008, **130**, 10870–10871.
41 S. J. Geier, J. A. Mason, E. D. Bloch, W. L. Queen, M. R. Hudson, C. M. Brown and J. R. Long, *Chem. Sci.*, 2013, **4**, 2054–2061.
42 J. A. Mason, M. Veenstra and J. R. Long, *Chem Sci.*, 2014, **5**, 32–51.
43 R. Sanz, F. Martinez, G. Orcajo, L. Wojtas and D. Briones, *Dalton Trans.*, 2013, **42**, 2392–2398.
44 K.-D. Liss, B. A. Hunter, M. E. Hagen, T. J. Noakes and S. J. Kennedy, *Phys. B*, 2006, **385–386**, 1010–1012.
45 A. J. Studer, M. E. Hagen and T. J. Noakes, *Phys. B*, 2006, **385–386**, 1013–1015.
46 B. H. Toby, *J. Appl. Crystallogr.*, 2001, **34**, 210–213.
47 A. C. Larson and R. B. Von Dreele, *Los Alamos National Laboratory Report*, LAUR 1994, pp. 86–748.
48 *SAINT and APEX 2 Software for CCD Diffractometers*, Bruker AXS Inc., Madison, WI, USA, 2009.
49 G. M. Sheldrick, *CELL_NOW*, University of Göttingen, Germany, 2008.
50 G. M. Sheldrick, *TWINABS*, University of Göttingen, Germany, 2009.
51 G. M. Sheldrick, *Acta Crystallogr.*, 2008, **A64**, 112–122.
52 G. M. Sheldrick, *SHELXS*, 2013, University of Göttingen, Germany.
53 O. V. Dolomanov, L. J. Bourhis, R. J. Gildea, J. A. K. Howard and H. Puschmann, *J. Appl. Crystallogr.*, 2009, **42**, 339–341.
54 T. J. Udovic, C. M. Brown, J. B. Leão, P. C. Brand, R. D. Jiggetts, R. Zeitoun, T. A. Pierce, I. Peral, J. R. D. Copley, Q. Huang, D. A. Neumann and R. J. Fields, *Nucl. Instrum. Methods Phys. Res., Sect. A*, 2008, **588**, 406–413.
55 R. T. Azuah, L. R. Kneller, Y. Qiu, P. L. W. Tregenna-Piggott, C. M. Brown, J. R. D. Copley and R. M. Dimeo, *J. Res. Natl. Inst. Stand. Technol.*, 2009, **114**, 233–241.
56 J. Perdew, K. Burke and M. Ernzerhof, *Phys. Rev. Lett.*, 1996, **77**, 3865–3868.
57 K. Lee, É. D. Murray, L. Kong, B. I. Lundqvist and D. C. Langreth, *Phys. Rev. B: Condens. Matter Mater. Phys.*, 2010, **82**, 081101.
58 G. Kresse and D. Joubert, *Phys. Rev. B: Condens. Matter Mater. Phys.*, 1999, **59**, 1758–1775.
59 P. E. Blöchl, *Phys. Rev. B: Condens. Matter Mater. Phys.*, 1994, **50**, 17953–17979.
60 V. I. Anisimov, J. Zaanen and O. K. Andersen, *Phys. Rev. B: Condens. Matter Mater. Phys.*, 1991, **44**, 943–954.
61 J. G. McDaniel and J. R. Schmidt, *J. Phys. Chem. A*, 2013, **117**, 2053–2066.
62 M. K. Rana, H. S. Koh, J. Hwang and D. J. Siegel, *J. Phys. Chem. C*, 2012, **116**, 16957–16968.
63 L. Valenzano, B. Civalleri, K. Sillar and J. Sauer, *J. Phys. Chem. C*, 2011, **115**, 21777–21784.
64 R. Poloni, B. Smit and J. B. Neaton, *J. Phys. Chem. A*, 2012, **116**, 4957–4964.
65 A. L. Dzubak, L.-C. Lin, J. Kim, J. A. Swisher, R. Poloni, S. N. Maximoff, B. Smit and L. Gagliardi, *Nat. Chem.*, 2012, **4**, 810–816.
66 P. Canepa, C. A. Arter, E. M. Conwill, D. H. Johnson, B. A. Shoemaker, K. Z. Soliman and T. Thonhauser, *J. Mater. Chem. A*, 2013, **1**, 13597–13604.
67 D. Yu, A. O. Yazaydin, J. R. Lane, P. D. C. Dietzel and R. Q. Snurr, *Chem. Sci.*, 2013, **4**, 3544–3555.
68 L. Wang, T. Maxisch and G. Ceder, *Phys. Rev. B: Condens. Matter Mater. Phys.*, 2006, **73**, 195107–195112.
69 P. Canepa, Y. J. Chabal and T. Thonhauser, *Phys. Rev. B: Condens. Matter Mater. Phys.*, 2013, **87**, 094407.
70 M. M. Märcz, R. E. Johnsen, P. D. C. Dietzel and H. Fjellvåg, *Microporous Mesoporous Mater.*, 2012, **157**, 62–74.
71 Z. B. Bao, L. A. Yu, Q. L. Ren, X. Y. Luand and S. G. Deng, *J. Colloid Interface Sci.*, 2011, **353**, 549–556.
72 R. Poloni, K. Lee, R. F. Berger, B. Smit and J. B. Neaton, *J. Phys. Chem. Lett.*, 2014, **5**, 861–865.
73 W. L. Queen, C. M. Brown, D. K. Britt, P. Zajdel, M. R. Hudson and O. M. Yaghi, *J. Phys. Chem. C*, 2011, **115**, 24915–24919.
74 P. D. C. Dietzel, R. E. Johnsen, H. Fjellvåg, S. Bordiga, E. Groppo, S. Chavan and R. Blom, *Chem. Commun.*, 2008, 5125–5127.
75 X. Kong, E. Scott, W. Ding, J. A. Mason, J. R. Long and J. A. Reimer, *J. Am. Chem. Soc.*, 2012, **134**, 14341–14344.
76 G. Mills, H. Jónsson and G. K. Schenter, *Surf. Sci.*, 1995, **324**, 305–337.
77 W. L. Queen, E. D. Bloch, C. M. Brown, M. R. Hudson, J. A. Mason, L. J. Murray, A. J. Ramirez-Cuesta, V. K. Peterson and J. R. Long, *Dalton Trans.*, 2012, **41**, 4180–4187.
78 H. Wu, J. M. Simmons, S. Gadiapelli, W. Zhou and T. Yildirim, *J. Phys. Chem. Lett.*, 2010, **1**, 1946–1951.
79 E. Haque and S. H. Jhung, *Chem. Eng. J.*, 2011, **173**, 866–872.